



Characterization of spherical AlSi10Mg powder produced by double-nozzle gas atomization using different parameters

Chao-feng GAO^{1,2}, Zhi-yu XIAO^{1,2}, Hai-ping ZOU^{1,3},
Zhong-qiang LIU^{1,2}, Jin CHEN⁴, Shang-kui LI³, Da-tong ZHANG^{1,2}

1. National Engineering Research Center of Near-Net Shape Forming for Metallic Materials, South China University of Technology, Guangzhou 510640, China;
2. Guangdong Provincial Key Laboratory for Processing and Forming of Advanced Metallic Materials, South China University of Technology, Guangzhou 510640, China;
3. Jiangxi Yuean Superfine Metal Co., Ltd., Ganzhou 341000, China;
4. Foshan Suizhibo Novel Materials Co., Ltd., Foshan 528000, China

Received 20 January 2018; accepted 14 September 2018

Abstract: A self-developed double-nozzle gas atomization technique was used to produce AlSi10Mg powder. Effects of delivery tube diameter, gas pressure, and melt superheat on powder characteristics were investigated. The concepts of bluntness and outgrowth were introduced to analyze powder sphericity and satellite index quantitatively. The results showed that the median diameters of all atomized powders ranged from 25 to 33 μm . The highest yield rate (72.13%) of fine powder ($<50 \mu\text{m}$) was obtained at a superheat of 350 K. The powder size decreased with increasing melt superheat but increased with increasing delivery tube diameter. Powders with bluntness values between 96% and 98% accounted for over 60%. The outgrowth values demonstrated that 70%–85% of all powders did not contain satellite particles, with few powders adhered two or three particles. Not only Al and Si phases were present but also a metastable Al_5Si phase was detected.

Key words: gas atomization; AlSi10Mg powder; particle size; particle shape; bluntness; outgrowth

1 Introduction

Many advanced forming technologies based on particulate materials, such as metal injection molding (MIM), thermal spray coating, and additive manufacturing (AM) [1], demand the availability of fine powder with a narrow particle size distribution [2,3]. This results in special requirements for the production of spherical powders or near spherical powders with narrow size distribution. Powder particles can be prepared by various methods, owing to the better kinetic energy transfer ability from gas to liquid metal, close-coupled gas atomization (CCGA) technique has been regarded to be one of the most important methods that developed in recent years.

The characteristic of metal powder is determined

mainly by the gas nozzle structure and the gas atomization parameters. Many studies have investigated the relation between powder properties and process parameters. METZ et al [4] found that increasing gas flow rate or gas pressure leads to a decrease in median particle size and the distribution range. AKSOY and ÜNAL et al [5] showed that the protrusion length of the melt delivery tube has little effect on the median powder size while the gas pressure is on the opposite. ACHELIS and UHLENWINKEL [3] proposed a new technique called pressure-gas-atomization (PGA) which results in a higher efficiency of atomization and a higher yield of the product.

However, few prior studies have been focused on the effect of powder shape distribution. In addition, standard protocols for powder characterization rely on sieve size distribution and light scattering methods which

Foundation item: Project (51627805) supported by the National Natural Science Foundation of China; Project (2015A030312003) supported by the Natural Science Foundation of Guangdong Province, China; Projects (2014B010129003, 2015B020238008, 2016B090931006, 2017B090901025) supported by the Science and Technology Research Department of Guangdong Province, China; Project (201604016049) supported by the Science and Technology Bureau of Guangzhou City, China

Corresponding author: Zhi-yu XIAO; Tel: +86-20-87110099; E-mail: zhyxiao@scut.edu.cn
DOI: 10.1016/S1003-6326(19)64947-2

provide only limited insight into the powder morphology. Generally, particle shape irregularity manifests at three main scales [6]: sphericity versus ellipticity or elongation in macroscale, roundness versus angularity in mesoscale, and roughness or smoothness in microscale, which involved the bluntness, roughness, outgrowth, and satellite [7]. In prior studies, ÖZBILEN [8] investigated satellite formation mechanism in gas atomized powder. WENTWORTH [9], a geologist, noticed that square rocks would gradually wear into spherical rocks, and then introduced the concept of bluntness. KRUMBEIN and SLOSS [10] designed a widespread bluntness chart for easy identification. It is known that both satellite and bluntness of powder particles have considerable influence on powder flow and bulk density [11]. In order to correlate the mechanical performance of metal powder with their intrinsic characteristics, it is essential to develop a precise method for the size and shape quantification. This work aims at providing a novel microscopic sensing technique relying on high-resolution image analysis to explore its potential for a better description of both the particles size and shape. Such results will be further correlated with classical physical testing methods to evaluate the predicting potential to be used as routine characterization methods in the quality control of gas atomization experiments.

2 Experimental

In this work, AlSi10Mg alloy ingots were used. The master alloys were prepared by induction melting at various temperatures ranging from 800 to 1000 °C in a corundum crucible. The molten alloy was poured into a tundish and then flowed into the delivery tube. The schematic diagram and the top view of the nozzle are shown in Fig. 1. The inner diameters of delivery tubes are 4.0, 4.2, 4.5, and 5.0 mm, respectively. Different atomization pressures (2.0–4.0 MPa) were used. The N₂ gas was preheated at 100 °C and the delivery tube was also preheated to keep the melt from freezing during the process. All atomization parameters are given in Table 1.

The as-atomized alloy powders were mechanically sieved to remove powder particles exceeding 150 μm in size. The size distribution of the powder was determined using a Malvern UK Mastersizer 2000. Particle shape parameters were measured by Occhio (Belgium) FC200S+HR particle shape analyzer, which used a high-resolution digital camera to obtain thousands of particle images and shape parameters. The elongation, bluntness, roughness, outgrowth and other morphological parameters of the particles were measured by CALLISTO grain analysis software.

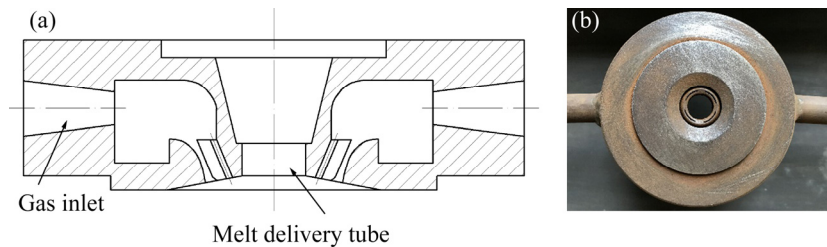


Fig. 1 Schematic diagram (a) and top view photo (b) of self-developed double nozzle

Table 1 Gas atomization parameters (Melting point of AlSi10Mg is about 650 °C)

No.	Delivery tube diameter/mm	Gas pressure/MPa	Melt superheat, T_s/K	Gas mass flow, $G_M/(kg \cdot min^{-1})$	Melt mass flow, $M_M/(kg \cdot min^{-1})$	Gas-to-metal ratio	Fine powder yield rate/%
1	4.2	3.0	200±5	29	2.43	11.93	63.16
2	4.2	3.0	150±5	29	2.46	11.78	65.82
3	4.2	3.0	300±5	29	2.50	11.6	64.43
4	4.2	3.0	250±5	29	2.59	11.12	64.85
5	4.2	3.0	350±5	29	2.52	11.6	72.14
6	4.2	2.5	250±5	18	2.60	6.92	63.46
7	4.2	4.0	250±5	54	3.48	15.51	65.29
8	4.5	3.0	250±5	29	2.70	10.74	65.56
9	4.0	3.0	250±5	29	1.21	23.97	69.82
10	4.2	3.5	250±5	42	3.00	14	65.56
11	5.0	3.0	250±5	29	3.03	9.57	65.24
12	4.2	2.0	250±5	10	1.88	5.32	60.51

Powder morphology was studied by scanning electron microscopy (SEM, FEI Quanta 200). For metallographic examination, the powder samples were cold resin mounted, polished with 1 μm diamond and etched subsequently with Keller's reagent (a solution of 2.5 mL HNO_3 , 1.5 mL HCl , 1 mL HF and 95 mL H_2O). Element distribution of the particle cross-section was examined by energy dispersive spectrometry (EDS). The phase of the powder was analyzed by X-ray diffraction (XRD, D8 ADVANCE) using $\text{Cu K}\alpha$ radiation, and the patterns were collected between 20° and 120° . The oxygen content of powder was measured with an oxygen–nitrogen analyzer (TC–500).

3 Results and discussion

3.1 Influence of melt delivery tube diameter

The effect of delivery tube diameter on the size of the produced AlSi10Mg powder is presented in Fig. 2. It is shown that the size distribution curves move to the right with increasing tube diameter, which means an increase of powder size. Increasing the metal flow rate from 1.21 to 3.03, the median particle diameter D_{50} is enhanced from 25.67 to 31.75 μm (Fig. 2(b)), and it can also confirm that a higher yield rate of fine powder leads to a smaller powder size. The atomized particle size D_m can be expressed as [4,12,13]

$$D_m = Kd[(1 + M_m/M_g)\eta_m/(\eta_g We)]^{1/2} \quad (1)$$

where K is an experimentally determined constant for particular conditions of spray and a liquid stream; d is the melt stream or the atomizer nozzle diameter; M_m and M_g are, respectively, the mass flow rates of the melt stream and the gas; η_m is the kinematic viscosity of the melt; η_g is the kinematic viscosity of the gas; We is the Weber number, which is defined as

$$We = v^2 \rho d / \sigma \quad (2)$$

where v is the gas velocity, ρ is the density of the metal, and σ is the surface tension of the liquid metal.

Since the gas pressure and the melt superheat were identical during the gas atomization process, it is clear that an increase of the delivery tube diameter leads to an increase of the melt mass flow rate (M_g), which may cause insufficient breakup of molten droplets. Generally, the whole gas atomization goes through three interrelated stages: primary breakup, secondary breakup, and solidification [14,15]. During the primary breakup, melt liquid column disintegrates into liquid film or ligament, and then develops instantly into droplets under the interaction of aerodynamic friction and surface tension [16,17]. As the primary breakup is finished, liquid droplets immediately undergo the secondary breakup. Only those melt droplets, whose Weber number

exceeds the critical value, can be broken up into fine droplets through different breakup modes in the secondary breakup [18,19].

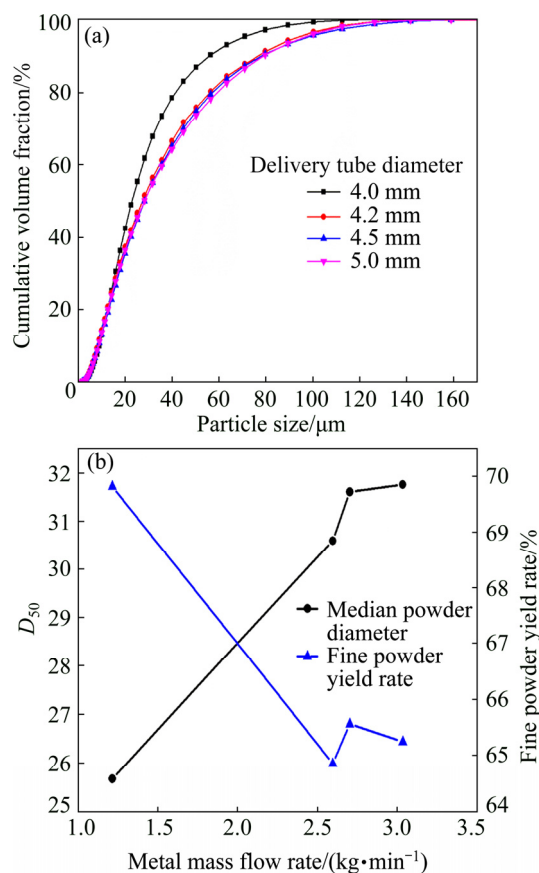


Fig. 2 Powder size distribution by using different melt delivery tube diameters (experimental conditions: pressure of 3 MPa and superheat of 250 K): (a) Cumulative volume fraction of particle size; (b) D_{50} and fine powder yield rate vs M_m

The SEM images of two different powders produced in different conditions are presented in Fig. 3. The powder generated with smaller melt delivery tube shows smooth and particularly fine particles (Fig. 3(a)) which agrees with the cumulative size distribution curve. Furthermore, agglomeration phenomena of fine particles are found in both powder images, which result from the strong interaction force between the fine powders.

In order to further understand the powder characteristics, multiscale analysis techniques were used to address the proper characterization of powder shape features. On the basis of MAURER et al [20], PIRARD et al [21] suggested to make use of the calypter and proposed an index (called bluntness index here) computed as follows:

$$W_V = \frac{1}{\sqrt{V}-1}, \quad \bar{V} = \frac{1}{N} \sum_{i=1}^{i=N} (1 + \frac{\lambda_E}{\lambda_i})^2 \quad (3)$$

where V is the particle volume, λ_E is the diameter of the maximum inscribed sphere (d_{IN}) and λ_i is the maximum

inscribed disc diameter (sphere in 3D) that containing the i th point of particle contour. In Occhio (Belgium) FC200S+HR particle shape analyzer, a perfect round particle has 100% bluntness. As shown in Fig. 4, powders with bluntness value above 95% are dominant, an increase of the delivery tube diameter leads to a significant reduction of powder bluntness, the median powder bluntness reduces from 77.2% to 65.1% as the delivery tube diameter increases from 4.0 mm to 5.0 mm (Fig. 4(b)).

The shape of the powder is ascribed to the gas atomization condition, e.g., solidification shrinkage, and various forces encountered in the flight course of the atomized droplets. Gas atomization is a complicated process, in which the kinetic energy of the atomizing gas is converted to the surface energy of the molten metal. According to the energy conservation law, with the increase of delivery tube diameter, the melt stream may not be sufficiently broken due to the increased melt flow rate. The kinetic energy of each droplet is significantly reduced, that is why the powder bluntness is reduced and the particle size is increased. What's more, the

spheroidization and solidification time are highly related to powder morphology. According to the former studies [22–24], for a given composition, the viscosity and surface tension of the molten droplets are approximately the same so that the spheroidization time only depends on the particle size. The fine droplet is always favorable for spheroidizing, while large ones are just on the opposite. For fine droplets spheroidization time is shorter than solidification time so that solid powder particles are spherical, while for large droplets solidification occurring before spheroidization is completed and thus leads to powder with irregular shapes.

In addition to the powder bluntness, satellite is also a significant factor affecting the property of the powder, especially powder flowability. The satellites are produced by collisions or impingement of fine solidified powder particles into the coarser molten or semi-molten particles during various solidification stages [3,8]. During atomization, large particles need more time to solidify than that of the finer ones due to the lower cooling rates. Furthermore, solidified finer particles

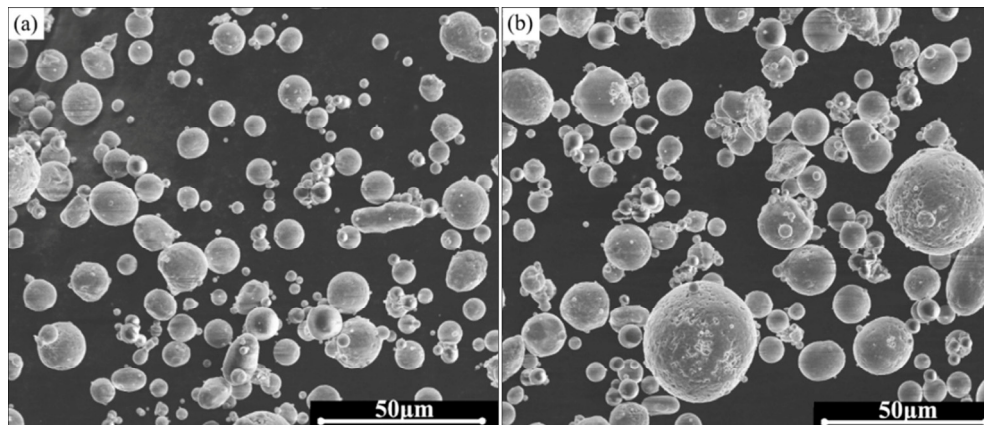


Fig. 3 SEM images of two different powders: (a) Sample No. 9 with melt delivery tube diameter of 4.0 mm, (b) Sample No. 11 with melt delivery tube diameter of 5.0 mm

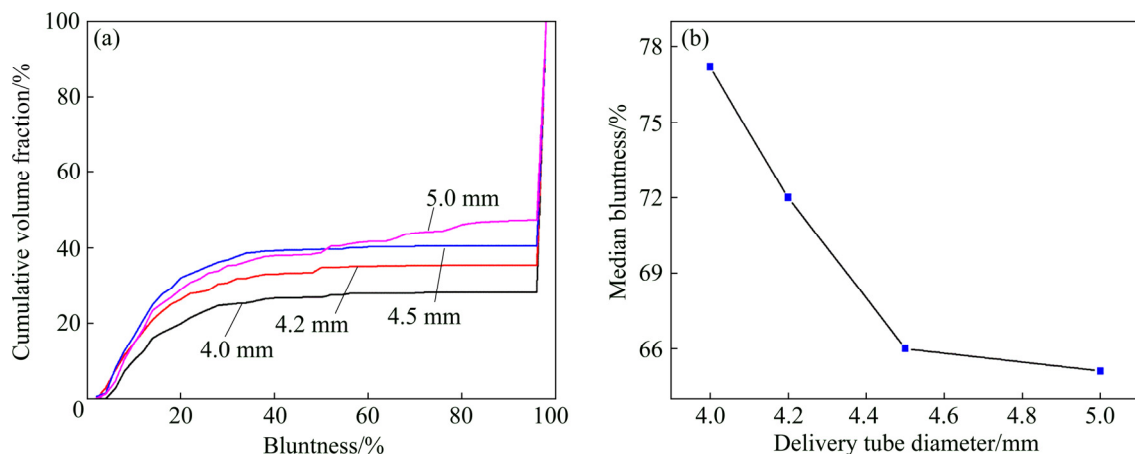


Fig. 4 Powder bluntness by using different melt delivery tube diameters: (a) Cumulative volume fraction of bluntness; (b) Median bluntness vs delivery tube diameter

move faster than the large particles and stick to the surface of large particles that are still in liquid form or in a mushy state. That's the satellite formation mechanism of gas atomized powder.

In the present work, satellite was discussed using a new concept called outgrowth (η), which is defined by Occhio:

$$\eta = 1 - \frac{1}{n_{\text{outgrowth}} + 1} \quad (4)$$

where $n_{\text{outgrowth}}$ is the number of outgrowth detected on the particle by using the particle shape analyzer. This formula points out that if a particle surface does not adhere to small particles, the outgrowth value is 0. Similarly, the outgrowth values of 50%, 66%, 75% or 80%, mean that the particle surface adheres to 1, 2, 3, and 4 small particle(s), respectively. As shown in Table 2, an increase in delivery tube diameter leads to a reduction in adhering particles, and the proportions of non-adherent particles are all above 76%. The powder atomized with a delivery tube diameter of 5.0 mm has the best surface morphology, about 84.86% particles are non-adherent, and only 14.29%, 0.83%, 0.02% particles adhere 1, 2 and 3 small particles, respectively.

The morphology of as-atomized powder and its representative particles are illustrated in Fig. 5. It can be seen that some larger particles are decorated with

Table 2 Proportion of non-adherent particles under different outgrowth values and melt delivery tube diameters

Delivery tube diameter/mm	Proportion of non-adherent particle/%				
	0%	50%	66%	75%	80%
4.0 (No. 9)	78.63	19.21	2.01	0.15	0
4.2 (No. 4)	75.88	22.1	1.99	0.03	0
4.5 (No. 8)	84.37	14.45	1.17	0.01	0
5.0 (No. 11)	84.86	14.29	0.83	0.02	0

satellites on the surface. Figures 5(b)–(d) show typical powder particles taken from Fig. 5(a) and their similar images (bottom left or right corner) obtained from Occhio (Belgium) FC200S+HR particle shape analyzer. The outgrowth values of these particles in Figs. 5(b–d) are 0, 50% and 50%, respectively.

A scatter plot of elongation vs roughness is drawn to present the shape distribution trend of powder (Fig. 6), where elongation is an indicator of the relationship between particle length and width while roughness describes the relative smoothness of particles [21,25]. It can be seen that most particles locate in the red box. Particles with low values of elongation and roughness mean high sphericity, as shown in the bottom left corner. On the contrary, particles having high values of elongation and roughness may be dumbbell-like or have

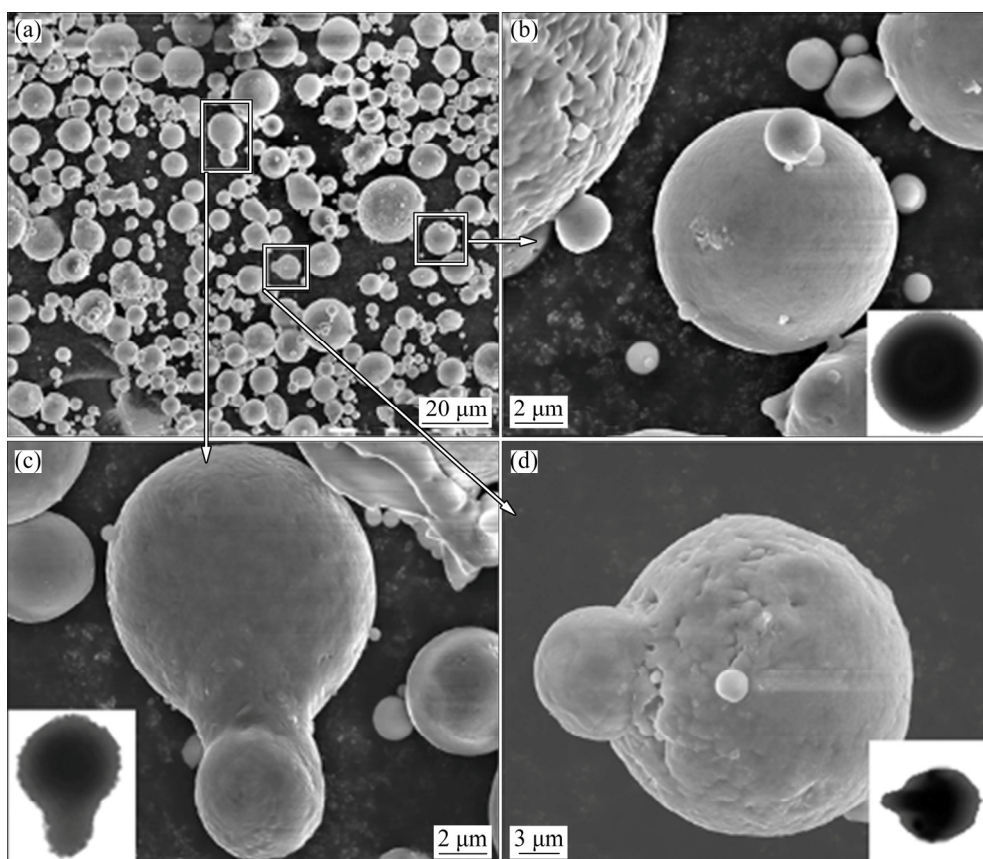


Fig. 5 Morphology of as-atomized powder (a) and representative particle morphologies (b–d) magnified from (a)

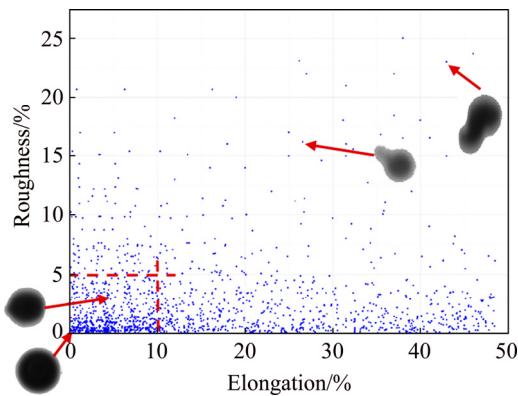


Fig. 6 Scatter plot of elongation vs roughness of powder of sample No. 9

satellites. By using the scatter plot, we can compare the shape distribution trend of the powders produced in different batches.

3.2 Influence of atomizing gas pressure

The influence of atomizing gas pressure on particle size and shape distribution has been studied at five levels (2.0, 2.5, 3.0, 3.5 and 4.0 MPa) with a constant superheat of 250 K and a melt delivery tube diameter of 4.2 mm.

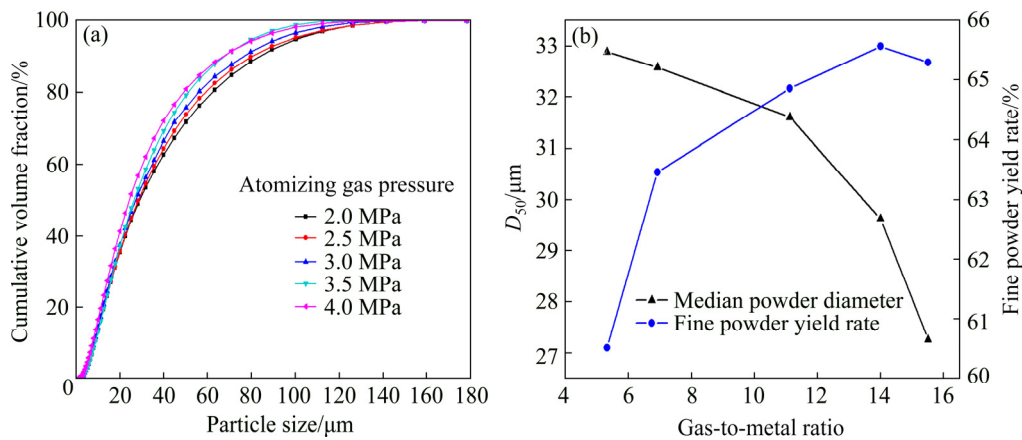


Fig. 7 Powder size distribution by using different atomizing gas pressures (experimental conditions: melt delivery tube diameter of 4.2 mm and superheat of 250 K): (a) Cumulative volume fraction of particle size; (b) D_{50} and fine powder yield rate vs GMR

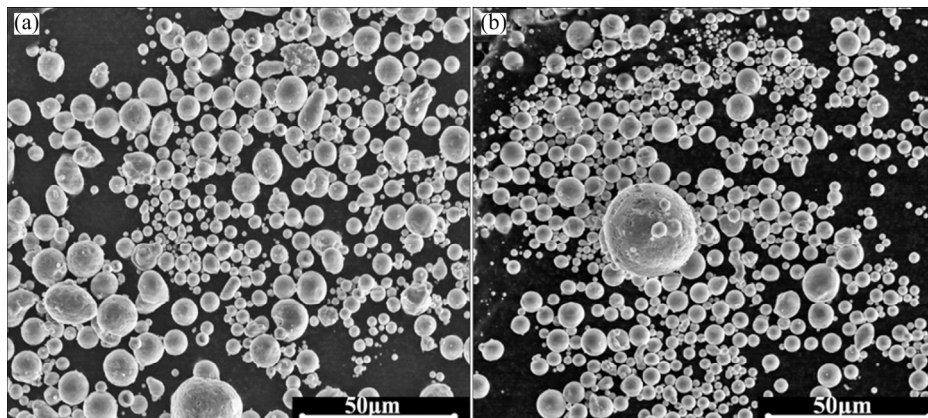


Fig. 8 SEM images of two different powders: (a) Sample No. 12 with gas pressure of 2.0 MPa; (b) Sample No. 7 with gas pressure of 4.0 MPa

The cumulative distribution and median diameter trends are shown in Fig. 7. As expected, the cumulative distribution curves move to left with increasing atomization pressure which means a reduction of powder size (Fig. 7(a)), median particle diameter D_{50} decreases with increasing gas to melt ratio (GMR) while fine powder yield rate is just on the opposite, as seen in Fig. 7(b). Previous research reported by TING et al [26] also showed that high GMR results in a reduction in median particle diameter D_{50} . ACHELIS and UHLENWINKEL [3] indicate that a gas mass flow between 100 and 300 kg/h leads to a higher product yield by using a pressure-gas-atomizer. Since the conditions of superheat were identical (250 K) in this part, according to Eqs. (1)–(2), the median particle diameter D_{50} only relates to gas to metal ratio (GMR). As seen in prior research, an increase in atomization gas supply pressure caused a steady increasing trend in gas mass flow. Meanwhile, the gas velocity would not be increased with pressure increase [2,27]. Data listed in Table 1 show the similar trend. The melt flow rate increases with the rise of gas pressure, which means that the bottom of the melt delivery tube is always in negative pressure state.

Figure 8 shows the morphology of two different

powders, and finer and spherical particles can be observed in Fig. 8(b). This confirms that the higher the atomization pressure, and the more sufficient breakup of the melt droplets, the smaller the particle size.

The bluntness values curves of the powders prepared under different gas pressures are presented in Fig. 9. Although the atomization pressure is changed, bluntness values from 96% to 98% accounted for the majority of the powder, which means that most of the powders have a high degree of sphericity (Fig. 9(a)). It can be seen that an increase in gas pressure from 2.0 to 4.0 MPa leads to an increasing trend of bluntness. Figure 9(b) shows a similar trend of median powder bluntness.

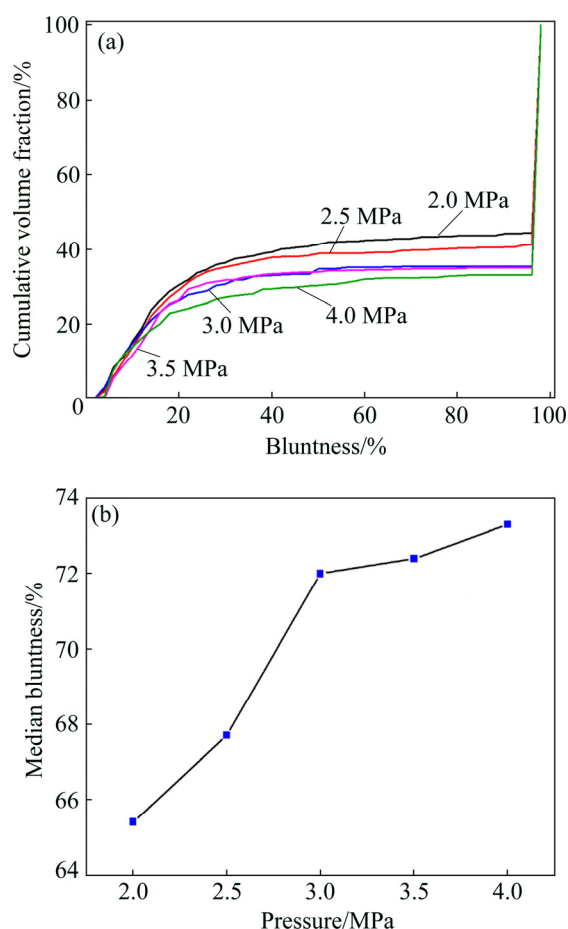


Fig. 9 Powder bluntness under different atomizing gas pressures: (a) Cumulative volume fraction of bluntness; (b) Median bluntness vs pressure

The increase of gas pressure strengthens the gas kinetic energy. Enough kinetic energy makes the breakup more sufficient, and the small droplets shrink into a spherical shape due to the surface energy. However, sufficient breakup means that more fine solidified powder particles are produced. These fine particles adhere to the coarser molten or semi-molten particles surface as a result of high-velocity airflow, and then these coarser droplets solidify to form satellite powders.

The differences in outgrowth values of the powder prepared under different gas atomization pressures are illustrated in Table 3. It can be seen that an increase in gas atomization pressure can increase the outgrowth value. The proportion of non-adherent particles decrease from 83.46% to 69.67% as the gas pressure increases from 2.0 MPa to 4.0 MPa.

Table 3 Proportion of non-adherent particles under different outgrowth values and atomizing gas pressures

Gas pressure/MPa	Proportion of non-adherent particle/%				
	0%	50%	66%	75%	80%
2.0 (No. 12)	83.46	15.45	1.02	0.07	0
2.5 (No. 6)	79.95	18.84	1.21	0	0
3.0 (No. 4)	75.88	22.1	1.99	0.03	0
3.5 (No. 10)	75.07	19.03	5.89	0.01	0
4.0 (No. 7)	69.67	27.43	2.88	0.02	0

3.3 Influence of melt superheat

The effect of melt superheat on the produced AlSi10Mg powder size is shown in Fig. 10. It can be seen from the size distribution curves (Fig. 10(a)) that the powder generated with the highest melt superheat (350 K) has the smallest particle size and the highest fine powder yield rate (Table 1). The median particle diameter (D_{50}) decreases with the increase of superheat (except 150 K), as seen in Fig. 10(b). A dramatical reduce in D_{50} can be found when the superheat increases from 300 to 350 K.

According to Eqs. (1)–(2), since the gas pressure and melt delivery tube were identical, the D_{50} is mainly related to melt surface tension, gas and melt kinematic viscosities. The relationship between the surface tension (σ_m) and the temperature of the metal melt can be expressed by [27,28]

$$\sigma_m \left(\frac{M}{\rho_m} \right)^{-2/3} = K(T_c - T) \quad (5)$$

where M is the molar mass of the metal melt, ρ_m is melt density, T_c is the critical temperature, and K is experimental constant. It is clear that the surface tension of the metal melt decreases as the temperature increases.

The melt kinematic viscosity (η_m) can be defined as

$$\eta_m = A \exp \left(\frac{E}{kT} \right) \quad (6)$$

where A is the pre-exponential factor, T is the thermodynamic temperature, E is the activation energy to move the flow unit in melt, and k is the gas constant.

The gas kinematic viscosity (η_g) which is called Sutherland's law has the following form:

$$\eta_g = \mu_0 \left(\frac{T}{T_0} \right)^{3/2} \frac{T_0 + S}{T + S} \quad (7)$$

where μ_0 is the reference value, T_0 is a reference temperature, and S is an effective temperature called the Sutherland constant.

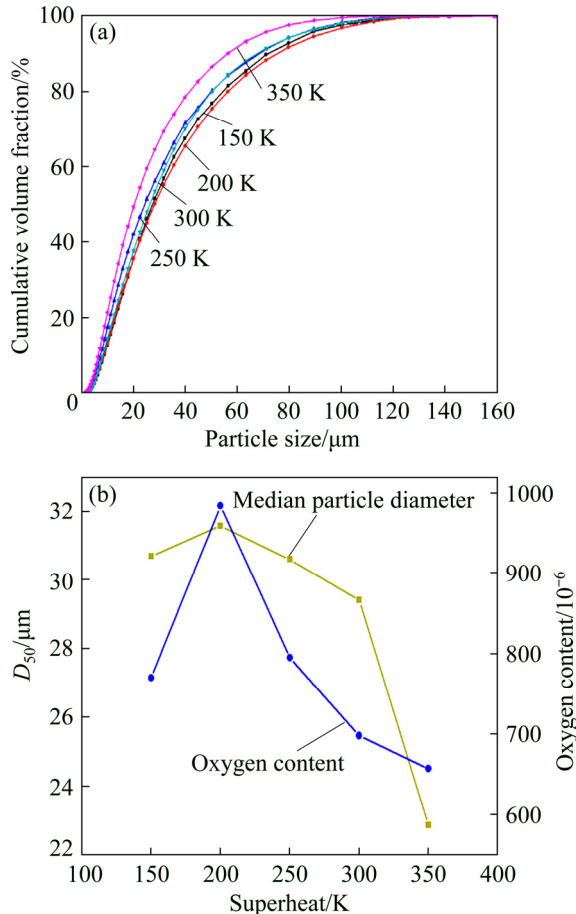


Fig. 10 Powder size distribution under different melt superheats (experimental conditions: melt delivery tube diameter of 4.2 mm and gas pressure of 3.0 MPa): (a) Cumulative volume fraction of particle size; (b) Melt superheat vs D_{50} and oxygen content

It is obvious that σ_m and η_m decrease with the increase of melt temperature while η_g is invariant since the gas temperature was identical. D_{50} decreases with the increase of melting temperature according to Eqs. (1)–(2). However, Fig. 10 shows the opposite trend at 150 K, in which the D_{50} is smaller than that at 200 K. This may be caused by the different oxygen contents during the melting period. It can be seen in Fig. 10(b) that the oxygen content first increases and then decreases sharply with the increase in temperature. A high oxygen content means that the melt is oxidized seriously, which increases the melt viscosity and thus leads to a larger powder size.

The SEM images of powder samples No. 1 and

No. 5 are compared in Fig. 11. A lower superheat may cause coarse particles, whereas, a higher superheat shows finer and smoother particles. Furthermore, both particles are not all spherical, satellite and agglomeration can also be seen.

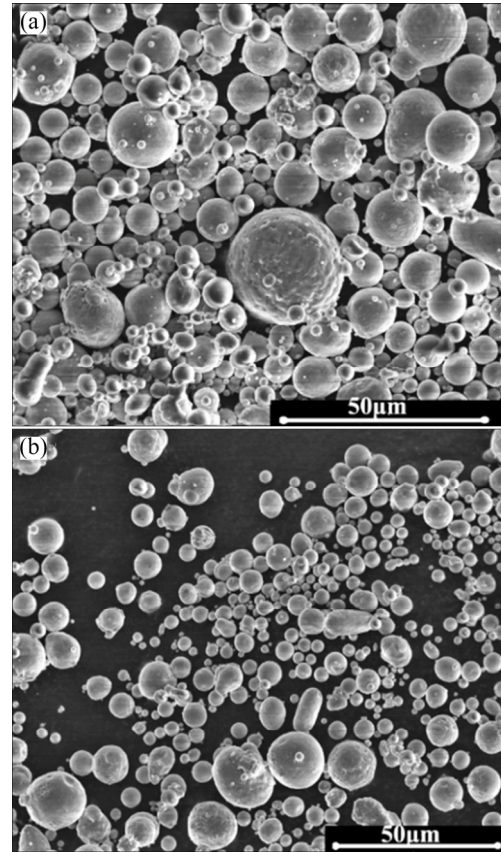


Fig. 11 SEM images of two different powders: (a) Sample No. 1 under melt superheat of 200 K; (b) Sample No. 5 with superheat of 350 K

Figure 12 shows the bluntness curves and median powder bluntness of the powders prepared under different superheats. The difference in bluntness values is not obvious, all the median powder bluntness values are above 70%, except sample No. 5 (superheat of 350 K). The SEM images confirm that although the powder of sample No. 5 (Fig. 11(b)) has finer particles, their roundness is not very good.

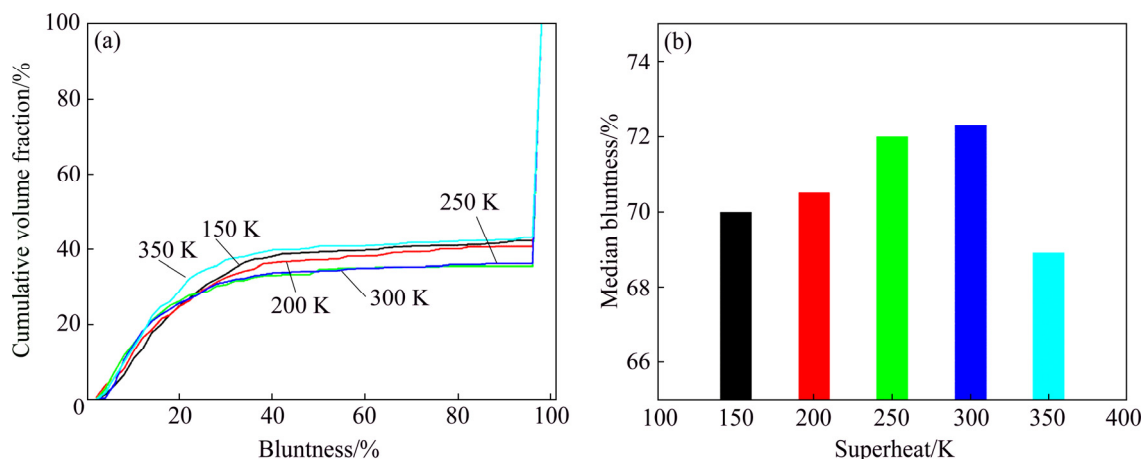
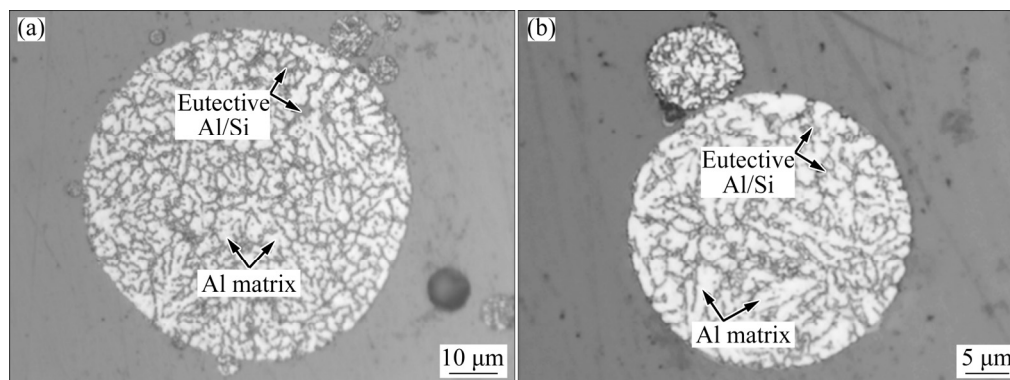
The outgrowth values of different powders do not show apparent regularity, as seen in Table 4. Non-adherent particles account for 83.83% of No.1 powder (superheat of 200 K), whereas, 69.32% of No. 5 powder (superheat of 350 K). No particles having four satellites (outgrowth values of 80%) are observed except for sample No. 5.

3.4 Microstructure and composition

Figure 13 shows the OM microstructure of etched AlSi10Mg powders. The cross-section microstructure

Table 4 Proportion of non-adherent particles under different outgrowth values and melt superheats

Melt superheat/K	Proportion of non-adherent particles/%				
	0	50%	66%	75%	80%
150 (No. 2)	76.62	21.44	1.94	0	0
200 (No. 1)	83.83	14.5	1.6	0.06	0.01
250 (No. 4)	75.88	22.1	1.99	0.03	0
300 (No. 3)	69.32	22.64	7.85	0.19	0
350 (No. 5)	77.4	20.29	2.28	0.03	0

**Fig. 12** Powder bluntness under different superheats: (a) Cumulative volume fraction of bluntness; (b) Median bluntness vs superheat**Fig. 13** OM images showing typical etched cross-section microstructure of AlSi10Mg powder

displays a supersaturated Al solid solution matrix with fine cellular-dendritic structure along with fibrous eutectic Al/Si at the cell boundaries.

The SEM images of the particle surface and cross-section of the AlSi10Mg powder are shown in Fig. 14. The solidified microstructure of cell structure and dendrites can be observed on the powder surface, as demonstrated in the blue and yellow boxes, respectively (Figs. 14(a) and (b)), this agrees with the results of the study reported by CHEN et al [29]. Microstructures of the powder cross-section are also conducted, and the results are presented in Figs. 14(d) and (e). It is found that the microstructure is similar to that of the powder surface, in which the cell structure and dendrites are easy

to be observed. Furthermore, small remaining pores are also found in the matrix, as illustrated by the black arrows, the atomization gas was entrapped in those powders.

The XRD patterns of the atomized powders and the EDS of the particle cross-section are presented in Figs. 14(c) and (f). Not only Al and Si phases can be detected, but also an Al_9Si phase presents which coincides with the characteristic peaks of Al. Due to the rapid solidification rate during gas atomization, the high cooling rate inhibits the precipitation of Si from the Al matrix to form a supersaturated solid solution Al_9Si , which is a metastable phase appearing in unbalanced solidification period that cannot be found in phase

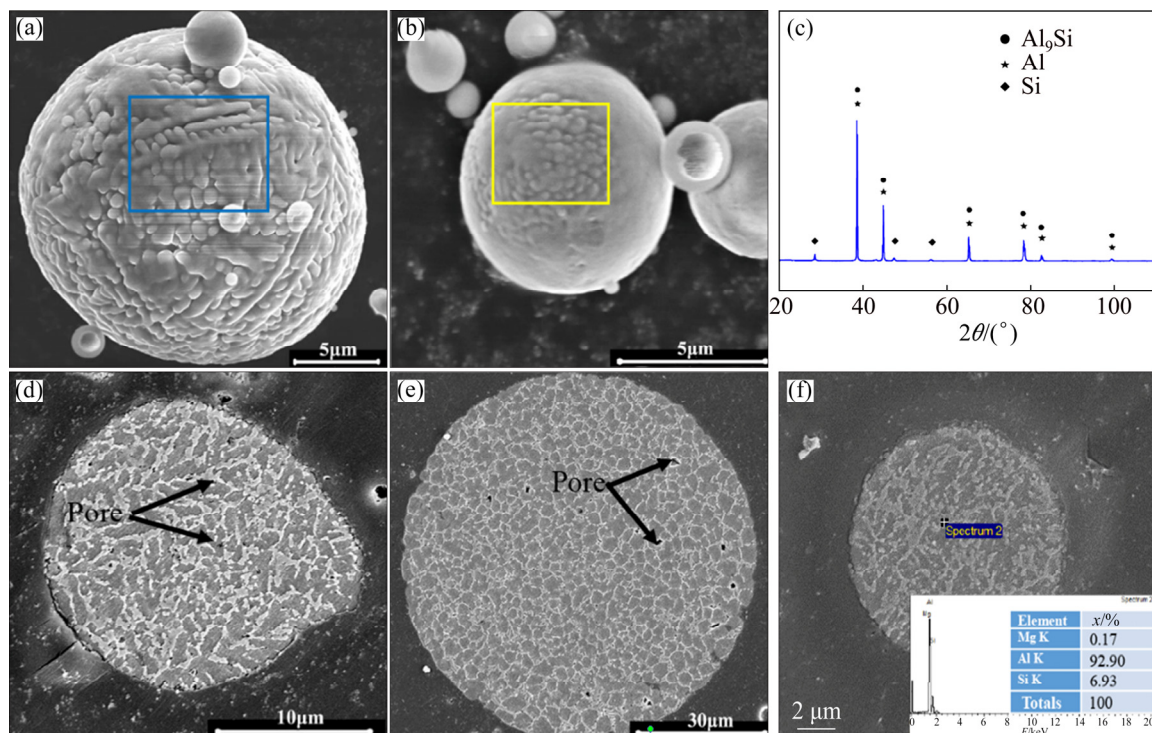


Fig. 14 SEM images of surface and cross-section microstructures of AlSi10Mg powder: (a, b) Surface morphologies; (c) X-ray diffraction pattern of atomized powder; (d, e) Cross-section microstructures; (f) EDS of atomized powder

diagrams. The EDS result shows that the content of Si in the Al matrix is 6.93%, which is higher than the equilibrium maximum solid solubility (1.65%) due to the high cooling rate (Fig. 14(f)).

4 Conclusions

(1) By using a self-developed double nozzle, the highest fine AlSi10Mg powder yield rate of 72.13% was obtained.

(2) An increase of gas pressure and melt superheat or a decrease of the tube diameter both led to a reduction of powder size, owing to the different melt mass flow rates and gas to metal ratio.

(3) Shape distribution results indicated that powders with similar median size might have significant differences in satellite and bluntness. Most of the produced powders had high sphericity with median bluntness values above 65%, and non-adherent powders accounted for 70%.

(4) A metastable phase of Al₉Si in addition to Al and Si phases was detected in the atomized powders.

References

- [1] YABLOKOVA G, SPEIRS M, van HUMBEECK J, KRUTH J, SCHROOTEN J, CLOOTS R, BOSCHINI F, LUMAY G, LUYTEN J. Rheological behavior of β -Ti and NiTi powders produced by atomization for SLM production of open porous orthopedic implants [J]. Powder Technology, 2015, 283(1): 199–209.
- [2] ANDERSON I E, TERPSTRA R L. Progress toward gas atomization processing with increased uniformity and control [J]. Materials Science and Engineering A, 2002, 326(1): 101–109.
- [3] ACHELIS L, UHLENWINKEL V. Characterisation of metal powders generated by a pressure-gas-atomiser [J]. Materials Science and Engineering A, 2008, 477(1–2): 15–20.
- [4] METZ R, MACHADO C, HOUABES M, PANSIOT J, ELKHATIB M, PUYANÉ R, HASSANZADEH M. Nitrogen spray atomization of molten tin metal: Powder morphology characteristics [J]. Journal of Materials Processing Technology, 2007, 189(1–3): 132–137.
- [5] AKSOY A, ÜNAL R. Effects of gas pressure and protrusion length of melt delivery tube on powder size and powder morphology of nitrogen gas atomised tin powders [J]. Powder Metallurgy, 2013, 49(4): 349–354.
- [6] POWERS M C. A new roundness scale for sedimentary particles [J]. Journal of Sedimentary Research, 1953, 23(2): 117–119.
- [7] BARRETT P J. The shape of rock particles: A critical review [J]. Sedimentology, 1980, 27(3): 291–303.
- [8] ÖZBILEN S. Satellite formation mechanism in gas atomised powders [J]. Powder Metallurgy, 1999, 42(1): 70–78.
- [9] WENTWORTH C K. The shape of pebbles [J]. Geological Survey Bull, 1922 (730): 91–114.
- [10] KRUMBEIN W C, SLOSS L L. Properties of sedimentary rocks [J]. Stratigraphy and Sedimentation, 1963: 106–113.
- [11] VLACHOS N, CHANG I T. Investigation of flow properties of metal powders from narrow particle size distribution to polydisperse mixtures through an improved Hall-flowmeter [J]. Powder Technology, 2011, 205(1): 71–80.
- [12] KAWAMURA Y, MANO H, INOUE A. Synthesis of ZrC/Zr55Al 10Ni5Cu30 metallic-glass matrix composite powders by high pressure gas atomization [J]. Scripta Materialia, 2000, 43(12): 1119–1124.
- [13] LUBANSKA H. Correlation of spray ring data for gas atomization of

- liquid metals [J]. JOM, 1970, 22(2): 45–49.
- [14] SEE J B, JOHNSTON G H. Interactions between nitrogen jets and liquid lead and tin streams [J]. Powder Technology, 1978, 21(1): 119–133.
- [15] DOMBROWSKI N, JOHNS W R. The aerodynamic instability and disintegration of viscous liquid sheets [J]. Chemical Engineering Science, 1963, 18(3): 203–214.
- [16] SHEIKHALIEV S M, BERYUKHOV A V, DUNKLEY J J. Metal droplet's deformation and break-up by a gas stream [C]//Proceeding of the world PM2004 Int. Conf., Vienna, 2004.
- [17] LEE C H, REITZ R D. An experimental study of the effect of gas density on the distortion and breakup mechanism of drops in high speed gas stream [J]. Int J Multiphase Flow, 2000, 26(2): 229–244.
- [18] JOSEPH D D, BELANGER J, BEAVERS G S. Breakup of a liquid drop suddenly exposed to a high-speed airstream [J]. Journal of Fluid Mechanics, 1996, 25(318): 1263–1303.
- [19] ORTIZ C, JOSEPH D D, BEAVERS G S. Acceleration of a liquid drop suddenly exposed to a high-speed airstream [J]. Int J Multiphase Flow, 2004, 30(2): 217–224.
- [20] MAURER C R J, QI R, RAGHAVAN V. A linear time algorithm for computing exact Euclidean distance transforms of binary images in arbitrary dimensions [J]. IEEE Transactions on Pattern Analysis & Machine Intelligence, 2003, 25(2): 265–270.
- [21] PIRARD E, CALIFICE A, LEONARD A, GREGOIRE M. Multiscale shape analysis of particles in 3D using the calypter [C]//10th European Congress for Stereology. Milano, 2009.
- [22] LAVERNIA E J, AYERS J D, SRIVATSAN T S. Rapid solidification processing with specific application to aluminium alloys [J]. International Materials Reviews, 1992, 37(1): 1–44.
- [23] ZHOU J, DUSZCZYK J, KOREVAAR B M. Structural characteristics of a nickel-modified Al–20Si–3Cu–1Mg alloy powder [J]. Journal of Materials Science, 1992, 27(12): 3341–3352.
- [24] CAI Z, WANG R, ZHANG C, PENG C, XIE L, WANG L. Characterization of rapidly solidified Al–27Si hypereutectic alloy: Effect of solidification condition [J]. Journal of Materials Engineering and Performance, 2015, 24(3): 1226–1236.
- [25] PIRARD E. Shape processing and analysis using the calypter [J]. Journal of Microscopy, 2011, 175(3): 214–221.
- [26] TING J, PERETTI M W, EISEN W B. The effect of wake-closure phenomenon on gas atomization performance [J]. Materials Science and Engineering A, 2002, 326(1): 110–121.
- [27] AYDIN O, UNAL R. Experimental and numerical modeling of the gas atomization nozzle for gas flow behavior [J]. Computers & Fluids, 2011, 42(1): 37–43.
- [28] NISHIMURA S, MATSUMOTO S, TERASHIMA K. Variation of silicon melt viscosity with boron addition [J]. Journal of Crystal Growth, 2002, 237(1): 1667–1670.
- [29] CHEN G, ZHAO S, TAN P, YIN J, ZHOU Q, GE Y, LI Z, WANG J, TANG H, CAO P. Shape memory TiNi powders produced by plasma rotating electrode process for additive manufacturing [J]. Transactions of Nonferrous Metals Society of China, 2017, 27(12): 2647–2655.

双喷嘴雾化技术制备球形 AlSi10Mg 粉末及其表征

高超峰^{1,2}, 肖志瑜^{1,2}, 邹海平^{1,3}, 柳中强^{1,2}, 陈进⁴, 李上奎³, 张大童^{1,2}

1. 华南理工大学 国家金属近净成形工程技术研究中心, 广州 510640;
2. 华南理工大学 广东省金属新材料制备与成形重点实验室, 广州 510640;
3. 江西悦安超细金属有限公司, 赣州 341500;
4. 佛山市岁之博新材料科技有限公司, 佛山 528000

摘 要: 采用自行研制的双喷嘴雾化技术制备 AlSi10Mg 合金粉末, 研究导液管直径、雾化压力、熔体过热度对粉末特性的影响, 引入钝度和赘生物指数概念来表征粉末球形度和卫星粉。结果表明: 所制备粉末的粒径中值在 25~33 μm 范围内, 在过热度为 350 K 条件下, 细粉(<50 μm)收得率最高达到 72.13%。粉末粒度随着熔体过热度的增大而减小, 随着导液管直径的增大而增大。钝度值为 96%~98%的粉末占总体的 60%以上。所有批次的粉末赘生物指数表明: 70%~85%的粉末没有粘连卫星颗粒, 只有极少量粉末粘连 2 个或者 3 个卫星颗粒。粉末组织中除 Al 和 Si 相存在外, 还有亚稳态的 Al₃Si 相生成。

关键词: 雾化; AlSi10Mg 粉末; 粒径; 粒形; 钝度; 赘生物指数

(Edited by Xiang-qun LI)